Flow Turbulence Combust (2016) 97:427–449
DOI 10.1007/s10494-016-9708-7

A Collaboration-based Approach to CFD Model Validation and Uncertainty Quantification (VUQ) Using Data from a Laminar Helium Plume

Weston M. Eldredge[1] · Pál Tóth[1] · Laurie Centauri[1] · Eric G. Eddings[1] · Kerry E. Kelly[1] · Terry A. Ring[1] · Axel Schönbucher[2] · Jeremy N. Thornock[1] · Philip J. Smith[1]

Received: 15 April 2014 / Accepted: 12 January 2016 / Published online: 2 February 2016

Abstract An effective approach to the model VUQ process by means of direct collaboration between computationalist and experimental data analyst is proposed. An analysis of data from a laminar helium plume experiment provides a demonstration of the proposed collaboration process. Consistency analysis serves a central role in the collaboration. It takes the data and uncertainties from both analyst and computationalist and provides an objective and quantifiable measure of agreement between the two. Despite the simplicity of the laminar helium system and the computational model, certain phenomena brought to light in the collaboration process make it difficult to find quantitative agreement in the data. These phenomena include the unsteady behavior of air flow in an open room, and the presence of helium permeation to the region near the plume. Important sources of error in the simulation include uncertainty in the room temperature (295.15 to 305.15 K), uncertainty in the helium inlet velocity (0.1215 $\frac{m}{s}$ to 0.1415 $\frac{m}{s}$), and uncertainty in local helium permeation (0 % to 3 % by mass.) The collaboration process allows for a better understanding of the phenomena affecting the plume and the relative sensitivities of the system to these phenomena.

Keywords Collaboration · Model validation · CFD · Data set consistency · Buoyant plumes

✉ Weston M. Eldredge
weseldredge@yahoo.com

[1] Institute for Clean and Secure Energy, University of Utah, Salt Lake City, Utah, 84112, USA

[2] Institute for Chemical Engineering I, University of Duisburg-Essen, Universitaetsstrasse 5, 45117 Essen, Germany

1 Introduction

Speaking of collaboration from the context of construction in civil engineering, East et al. offer the following definition: "Collaboration is defined as working together on a joint intellectual effort. The ability to work collaboratively depends upon knowing the people involved, trusting that each party is fully participating, knowing how to find the resources needed to work together, and being able to compromise in order to achieve mutually agreed upon results" [1]. Collaboration among diverse disciplines is a common and effective paradigm for achieving greater progress in various research endeavors. Specifically, in Computational Fluid Dynamics (CFD) the process of model validation and uncertainty quantification (VUQ) necessitates at least some degree of collaboration between computation and experiment as comparison of computational predictions with experimental data forms the basis of nearly all VUQ methods. There are several definitions of model VUQ in the literature [2–7]. This paper seeks to demonstrate a novel approach to collaborative model VUQ.

The most basic (and minimal) type of collaboration in model VUQ occurs when the model developer compares their model predictions with data found in the literature. Such comparisons often involve little or no communication with the experimentalist, and sources of error/uncertainty from both computation and experiment are not thoroughly analyzed. Also, in most data comparisons found in the literature the degree of agreement between computation and experiment are not determined quantitatively, but they are subjectively qualified as "good" or "reasonable" [8–16], and [17]. A more collaborative approach to VUQ could rectify these issues and allow a quantitative measure of data agreement. In contrast to this basic VUQ approach, a number of examples of more collaborative based efforts are found in the literature. These include efforts to produce and compile collections of high quality (low uncertainty) experimental data for the purpose of model VUQ [18–23], and [24], VUQ efforts with grid computing [25] and [26], and collaborative VUQ workshops [27].

The present study seeks to further implement the concept of collaboration in model VUQ. In this case the collaboration is between a computational group and a data analysis group using experimental data from the literature. In this case both the modeler and the analyst can respond to shortcomings in their methods revealed in the collaboration process and revise their analysis and update their predictions. Both parties can also update estimates in the uncertainties inherent to their methods. The present collaboration is limited in that the experimental team cannot exercise this same flexibility. Much is known about the conditions of the experiment and the uncertainties in experimental conditions from both published data and from communication with the experimentalist, but any flaws in the experiment cannot be remedied by returning to the lab to adjust the experimental conditions or from making new measurements. The available data must stand as they are. The data are a series of holographic images of a laminar helium plume experiment [28]. Helium systems are examples of simple buoyant flow systems that are frequently studied to obtain data for model VUQ [19, 29–31], and [23]. ARCHES is the code that provides the computational data for the study [32]. The helium plume system provides a simple subject for the collaborative model VUQ that is free of the complexities of turbulence that would otherwise complicate measurements and introduce error in the computational predictions from closure models. An important tool in the collaboration is the Data Collaboration (DC) software that Feeley et al. describe [33]. The DC tool uses the uncertainty from the experiment, the data analysis of the holographic images, and the computational results to provide an objective and quantitative measure of agreement among these data types. In future references to the DC

software, it is important to distinguish between the collaboration between data analyst and computationalist, which is the primary subject of this study, and the Data Collaboration software (which will be referred to as DC software or simple DC to avoid confusion.) The objective of this study is to show that by working more directly together the analyst and the computationalist can accomplish more to (1) quantify the error in the computational predictions, (2) gain greater insight into the experimental procedure, instrumentation, and conditions, as well as the capabilities of the data processing tools, and (3) acquire a better understanding of the physical system of interest.

2 Methods

2.1 Collaboration objective: The quantity of interest

An important step in the collaboration process is the selection of a quantity of interest, which is something that the experimentalist can measure, or in this case the analyst can derive from the experimental data, and the computationalist can produce, with minimal error from each party. The quantity of interest for this study is the time-averaged phase shift between the two laser beams used to generate the holographic images at various locations in the helium plume. To produce the phase shift from simulation data the optical path length difference relation is needed:

$$\Psi(x, y) = \frac{2\pi}{\lambda} \int [n_m(x, y, z) - n_0]\, dz. \tag{1}$$

In this equation, $\Psi(x, y)$ is the phase shift (at location (x, y)). The symbol $n_m(x, y, z)$ represents the refractive index of the fluid at a point in the domain, and n_0 is the reference refractive index for pure air at experimental conditions. The wavelength of the laser is λ. Once the data analyst processes the images, each holographic interferogram provides phase shift data over a two-dimensional domain. Because the composition of helium varies throughout the plume, the phase shift values vary over the image surface. The collaboration examines the time-averaged (over two seconds) phase shifts at 1296 locations over the image surface. These locations include 36 points distributed horizontally (the horizontal direction indicated by the y-coordinate) across the plume beginning 24.15 millimeters to the left of the plume center and extending 24.15 millimeters to the right of the plume center. This distribution of points occurs at 36 different heights of the plume (the vertical indicated with the x-coordinate), which extends from 0.69 millimeters above the inlet to 48.99 millimeters above. This distribution of points covers the view of the holographic interferograms.

2.2 Simulation

A multi-physics, multi-scale, massively-parallel, Large Eddy Simulation (LES) code called Arches performs the computations needed for the simulation aspect of the quantitative study [32]. The Arches code is easily adapted for simulation of the laminar, buoyant helium plume system that is of interest here. Arches applies the conservative, finite-volume, compressible form of the Navier-Stokes equations. For the helium plume simulations the equations of interest include the integral form of the mass, momentum, and mixture fraction balances. As the helium plume system is assumed isothermal, the energy balance is not considered.

The Arches code uses second-order spatial discretization for the momentum equation. Flux limiters are used for the convective terms in the mixture fraction transport. An explicit

Runge-Kutta scheme ($O(2)$) advances the solution forward in time. A simple two-stream mixing approach determines the fluid density,

$$\frac{1}{\rho_{mix}} = \frac{f}{\rho_{he}} + \frac{(1-f)}{\rho_{air}}. \tag{2}$$

The Arches algorithm first advances the mixture fraction equation in time as,

$$(\rho f)^{n+1} = (\rho f)^n + RHS(\rho^n, f^n)\Delta t, \tag{3}$$

where RHS represents the discrete right-hand-side of the mixture fraction equation including diffusion and convection and Δt is the discrete timestep. The implicit dependence of the density and mixture fraction from Equations 2 and 3 is resolved by approximating the density at $n+1$ using a density guess, ρ^*, obtained from a simple time-advancement of the continuity equation,

$$\rho^* = \rho^n + D(\rho^n, \mathbf{U^n})\Delta t, \tag{4}$$

where $\mathbf{U}$ is the velocity vector and D is the discrete divergence operator. The updated mixture fraction is then approximated as, $f^{n+1} \approx (\rho f)^{n+1}/\rho^*$. Equation 2 is subsequently used to determine ρ^{n+1}. The approximation to the mixture fraction/density relationship is not repaired as the solution advances and represents a potential source of numerical error. Given the absence of any combustion or turbulence, the simulation output is particularly sensitive to this algorithmic approximation. If the error of this approximation is substantial, the data-collaboration will highlight it as such.

To produce the quantity of interest the simulation outputs of local helium mass fraction ($\bar{\gamma}_i(x, y, z)$) and fluid density ($\rho_m(x, y, z)$) are used to calculate the phase shift through the Gladstone-Dale (5), and the optical path length difference equation (Equation 1).

$$n_m(x, y, z) = \frac{3}{2}\left[\frac{1}{\rho_m(x, y, z)}\right]\frac{\sum_i \bar{\gamma}_i(x, y, z)\, N_i^0}{\sum_i \bar{\gamma}_i(x, y, z)} + n_0. \tag{5}$$

The x-axis is the vertical (axial) coordinate, the y-axis is horizontal (radial), and the z-axis (laser-path through the plume) is orthogonal to the other two. The Gladstone-Dale equation provides refractive index ($n_m(x, y, z)$) as shown in Eq. 5 using the specific standard refractivity of species i (N_i^0) (the species in this case are air or helium) and pure air refractive index (n_0). The optical path length difference equation (Equation 1) provides the phase shift, $\Psi(x, y)$ by integrating along the laser path length (z-axis) through the plume [34].

Figure 1 shows a plot of density data from a helium simulation, and it shows the computational domain used for the helium plume simulations. The domain models the helium inlet as a velocity boundary condition with the velocity set to a single, uniform value for the whole inlet. The composition at the inlet is pure helium, and the inlet is circular in shape with a 4.6 centimeter diameter. The domain is a cube with side length of 13.8 centimeters (three times the diameter of the plume inlet). The boundary condition at the top of the domain is modeled as an outlet, and the sides of the domain are pressure boundaries. This arrangement of boundary conditions allows flow out the top and entrainment of air through the sides. The bottom face of the domain not covered by the inlet is another inlet that injects air at a set velocity. This is done to model the conditions of an open environment without having to model the entire room where the experiment takes place.

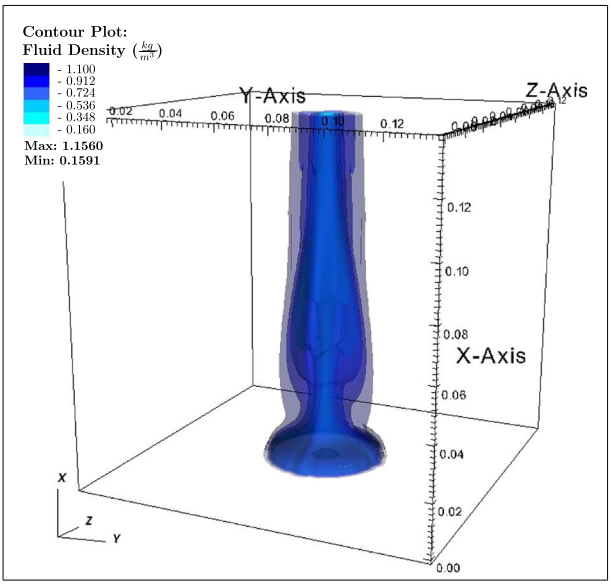

Fig. 1 This image shows a 3-dimensional, fluid density (in kg/m^3) plot of the helium plume system from a simulation. The entire simulation domain is included. The numbers along each of the three axes are in units of meters. All three dimensions are of the same length (0.138 meters.) The heavier, air-dominated regions are made transparent to show the boundaries of the plume. The inlet at the bottom of the domain is circular with a diamter of 4.6 cm

Each simulation is run for a time (simulation time) of 6.0 seconds. This is long enough to allow the plume to reach a steady pulsing behavior. The last two seconds of the simulation are used for data extraction and for the time-averaging of the phase shifts. Each simulation requires about 8 hours of real time to complete and requires 64 processors in parallel. The grid is structured Cartesian, and the resolution is 100^3 computational nodes (Δx, Δy, Δz = 1.38 mm.)

In regard to code verification, Arches is routinely tested via various manufactured solution methods, so further code verification is not performed. For solution verification, three helium simulations are run at different resolutions. Comparisons of data at three resolutions (80^3, 100^3, and 125^3 nodes) show negligible difference. Therefore, discretization error is not considered a major source of error.

2.3 Model uncertainty parametrization and design of simulations

Another important part of the collaboration process is identifying and quantifying of the sources of error in the model and the seeing how these error sources propagate to the error in the model predictions. The potentially important sources of error in this case arise from the modeling of the open system through the application of certain boundary conditions and the uncertainty in variables related to experimental conditions (called *scenario parameters*.) Scenario parameters considered here include the helium inlet velocity, the temperature of the system, the velocity for the co-flow boundary, the wavelength of the laser used to generate the holographic images, and the concentration of residual helium in the vicinity near the plume. The uncertainty in the helium inlet velocity is assumed to be ± 10 % of the average

measured value of 0.135 meters per second. The chosen range of uncertainty for the system temperature (295.15 to 305.15 Kelvins) is based on weather records for the date and location of the experiments [35]. Temperature influences the helium system through the rate of molecular diffusion. Higher temperatures produce faster diffusion rates. For the helium/air system the following values of the binary diffusivity are used: At 295.15 K the diffusivity is $7.1248 \times 10^{-5} m^2/s$, for 300.15 K the value is $7.3273 \times 10^{-5} m^2/s$, and at 305.15 K the diffusivity takes a value of $7.5320 \times 10^{-5} m^2/s$. The diffusivity values are estimated from a method that gives errors as high as 2 % for the helium/air system in the temperature range of interest [36]. The appropriate range for co-flow velocity is estimated to be from 10 % to 50 % of nominal helium inlet velocity. The laser wavelength uncertainty is assumed to be ± 5 nanometers. Finally, the range of values considered for helium permeation range from 0 % (clean air) to 3.2 % by mass. A summary of these scenario parameters with their uncertainty ranges is given in Table 1.

With these scenario parameters identified, the next step is to see how their uncertainties affect the range of values in the predicted phase shifts at each point of the plume. Several helium simulations are run using different values for the scenario parameters to generate a response surface for the time-averaged phase shift. No more than four of the five scenario parameters listed in Table 1 are considered at a given time. Some parameters turn out to have a weaker influence on the results than others. With three or four parameters the number of simulations needed for a response surface can quickly become cumbersome. A Box-Behnken experimental design minimizes the number of simulations required [37]. With an appropriate response surface values for the quantity of interest can be accessed for the whole input parameter space using a robust interpolation method. Gaussian Process Regression (GPR) fulfills this role for the present study [38].

2.4 Experimental data set

The collaboration focuses on holographic interferograms taken from laminar helium plume experiments in which helium emerges from a 4.6 centimeter (diameter) port and mixes with the surrounding air as it rises [28].) Holographic interferometry provides a non-intrusive means to analyze buoyant plume systems. The details concerning how the holographic images are produced can be found in [39]. In brief, one laser beam (the object beam) passes through the helium plume while another beam (the reference beam) is passed through clean air. When the two beams are combined they are out of phase due to the difference in refractive index between helium and air. This difference in phase creates interference patterns on the images. The interference patterns encode the projected gradient of the refractive index for each part of the region that the laser passes. A higher density of fringes in the image

Table 1 This table lists the experimental scenario parameters thought to be the most likely to contribute to the uncertainty in the simulation prediction of the phase shift data

Parameter	Lower limit (α)	Nominal	Upper limit (β)
Temperature, (K)	295.15	300.15	305.15
Helium velocity, ($\frac{m}{s}$)	0.1215	0.135	0.1485
Air co-flow, ($\frac{m}{s}$)	0.0135	0.0405	0.0675
Laser wavelength (nm)	509.15	514.15	519.15
Helium permeation (% by mass)	0 %	1.6 %	3.2

indicates a higher refractive index gradient. Because the changes in refractive index are due to changes in helium concentration, the fringe patterns in the holographic interferograms provide information about the composition of the plume and its mixing patterns.

Figure 2 shows an example of a holographic interferogram from the laminar helium experiments and a corresponding fringe pattern produced from a helium simulation. Note that the regions of the plume where helium concentration (and refractive index) changes rapidly, such as the base of the plume, have a higher density of fringe lines, and the areas of the plume with smaller concentration gradients, such as the top regions of the image and the sides of the plume, have fewer fringes. Holographic interferometry is commonly used for study of different plume systems as well as for model VUQ [23, 34, 40–43], and [39].

2.5 Phase shift extraction from digital holographic interferograms

The holographic interferograms arise from experiments, but the phase shift data used for model comparison is the result of image processing on the part of the analyst. The sources of error associated with the experimental phase shift data arise from both the conditions of the experiment as well as from elements of the image processing. The holographic interferograms are digitized in TIF format (1920 X 1080 pixels, 8 bit). Each set consists of approximately 2000 holographic interferograms. The holographic interferograms are obtained at a frame rate of 1000 images per second, meaning that the durations of recordings are about 2 seconds. This time interval contains 15 puff cycles on average.

In the pre-processing step, the holographic interferograms are cropped, and a common spatial coordinate system is defined in which each image is positioned. The coordinate system is located by robustly fitting a circle over the outlines of the laser spot, which is assumed to be stationary relative to the helium outlet during the experiments. This spatial registration step is necessary to correct for the random displacements of manual digitization.

The following equation represents interferometric fringe patterns:

$$i(x, y) = a(x, y) + b(x, y) \cos[\psi(x, y)] + N(x, y), \tag{6}$$

where $i(x, y)$ is a two-dimensional scalar (intensity) image, $a(x, y)$ and $b(x, y)$ are low-frequency background bias and fringe contrast terms, $\psi(x, y)$ is the underlying projection of the phase shift map and N(x,y) is a (usually) high-frequency noise term. The quantity of

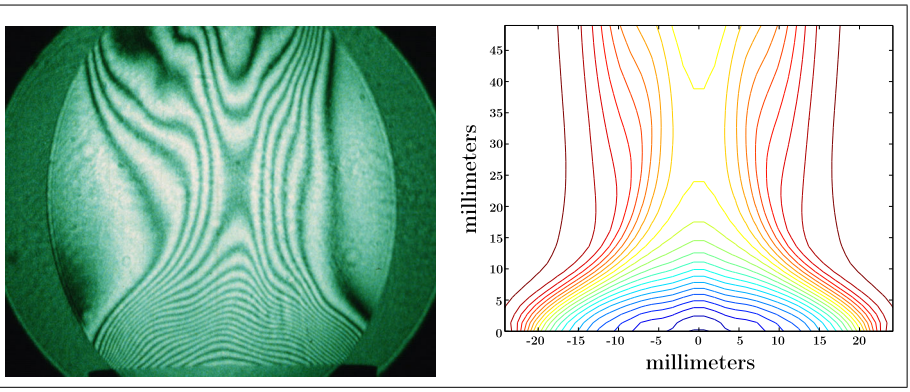

Fig. 2 The left image is an example of a holographic interferogram from the experimental data of [28], and the right image is a computational reproduction of the same experiment

interest, the total shift in the phase of the measurement beam relative to the reference beam can be extracted from the interferograms by demodulating $\cos[\psi(x, y)]$ - in other words, reverse engineering the cosine dependency. This demodulation step must be reasonably robust to the terms $a(x, y)$, $b(x, y)$ and $N(x, y)$. A method based on the isotropic quadrature transformation [44] and [45] and unwrapped fringe orientation estimation [46] is used. This method computes ψ from normalized fringe patterns, that are produced by adaptive filtering [47]. Due to the periodicity of the cosine function, the demodulation process generated maps of $\psi(x, y)$ modulo 2π. This phase shift map, with values bounded between 0 and 2π is called the wrapped phase. The lost information in the modulation-demodulation process can be reacquired by unwrapping the wrapped phase. The following equation describes the unwrapping procedure:

$$\Psi(x, y) = \psi(x, y) + m(x, y)2\pi, \tag{7}$$

where $\Psi(x, y)$ again represents the unwrapped phase, and $m(x, y)$ is a map of integers. The unwrapping procedure finds $m(x, y)$ and removes modulo 2π discontinuities in the phase map. Note that due to the symmetry of the cosine function, the gradient direction in $\nabla\psi$ is ambiguous and cannot be exactly determined from a single fringe pattern. A multi-grid minimization method estimates $\Psi(x, y)$ [48].

Two free parameters arise in the methodology outlined above, both due to the orientational vector-field regularization used to obtain the modulo 2π fringe orientation, which is used in the demodulation process to estimate the phase gradient direction. A computation of the gradient orientation of $i(x, y)$ yields a first approximation of fringe orientation:

$$\theta(x, y) = \tan^{-1}\left(\frac{\partial i(x, y)/\partial x}{\partial i(x, y)/\partial y}\right), \tag{8}$$

which is modulo π due to the sign ambiguity of the arctangent function. To produce a useful orientation measure that can guide the determination of the sign of $\nabla\psi(x, y)$, a θ modulo 2π is required. Omitting derivation and following the notation of [46], the minimization of the following cost function produces the desired changes.

$$U_r(n) = \sum_{\overline{r}\in\Gamma}\left\{[\Theta(\overline{r})\cdot n(r)]^2 + \mu\,[n_x(r) - n_x(\overline{r})]^2\, s(\overline{r}) + \mu\left[n_y(r) - n_y(\overline{r})\right]^2 s(\overline{r})\right\}, \tag{9}$$

where $r = (x, y)$ and $\overline{r} = (\overline{x}, \overline{y})$ are the location vectors and the mean of location vectors in a local region Γ, $\Theta(r) = \{\cos(\theta(r)), \sin(\theta(r))\}$, $n(r)$ is the normal vector field subject to regularization, $n_x(r)$ and $n_y(r)$ are the already regularized vectors in the local neighborhood Γ, $s(r)$ is a Boolean function with true values in already regularized locations and μ is the regularization parameter. The two free parameters arising from this formulation are the size of the neighborhood Γ and μ, both controlling the smoothness of the regularized vector field. In short, this regularization technique relaxes the local normality criterion $\Theta(\overline{r})\cdot n(r)$ to find an unambiguous modulo π orientation map. For further details, the reader is referred to [46].

This algorithm is applied to batch-process the interferograms, and the unwrapped phase maps are saved. Some functionality of the XtremeFringe library [49] is used to process images. Figure 3 demonstrates the steps taken in processing the interferograms. Time-average phase maps are computed from the instantaneous measurements. In the next step, the coordinate systems of the experiment and simulation are matched by using the helium outlet as a reference. The resolution of the experimental measurements is higher than that of

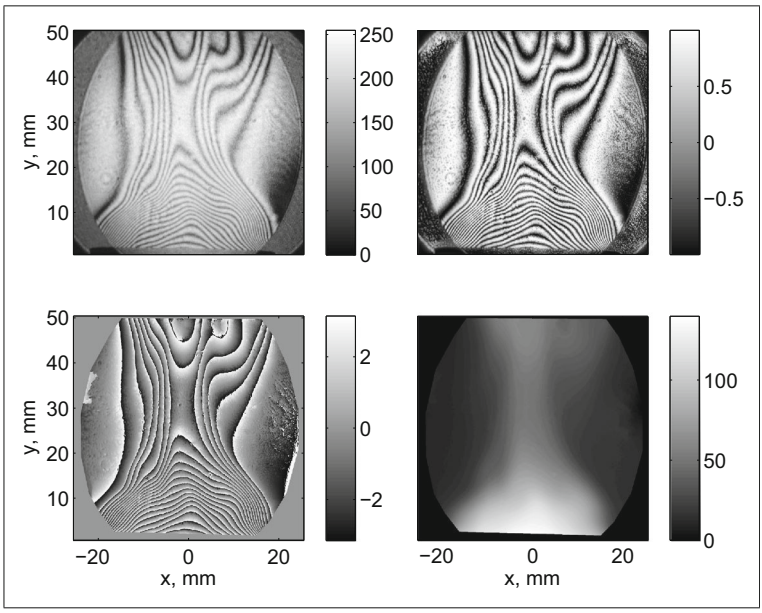

Fig. 3 A demonstration of the image processing procedure. Top left: registered interferogram. Top right: normalized interferogram. Bottom left: demodulated phase ψ. Bottom right: unwrapped phase Ψ

the simulation grid, thus the phase maps are sub-sampled so that the resulting low-resolution maps match the simulation grid. Details of the simulation grid are found in the next section.

Uncertainties in the image processing step include:

1. The uncertainty caused by registration error. This arises from imperfect image alignment and sub-sampling error. The magnitude of the uncertainty is estimated to be one simulation grid. This is handled as random error.
2. The uncertainty caused by insufficient image resolution. In locations where a high frequency of fringes are found, digital images are not always able to resolve every fringe. In other words, the Nyquist criterion is not met for sampling the fringe pattern at these locations. This leads to lost fringes in the normalized images and a lower gradient magnitude in ψ. Ultimately, the unwrapped phase Ψ is underestimated in these regions. This phenomenon is classified as systematic error.
3. The uncertainty caused by image degradation. This includes digitization artifacts, image noise, the term $a(x, y)$ in Eq. 6, the slight warping of the holographic film, etc. Generally, every image feature that is not part of the fringe pattern is classified as degradation. These image features result in a systematic overestimation of Ψ and thus are handled as systematic error.
4. The uncertainty caused by the erroneous estimation of the direction of $\nabla\psi$. Although the unwrapped phase is constrained to estimate the typical jet-like phase map of the plume, the regularized solution is not always correct. In some cases, the unwrapped maps locally show unrealistic distributions. As an example, this causes a mean error of 2π radians in Ψ in the case of one incorrectly detected fringe cycle. This effect may also cause sharp jumps in the time series of phase measured at a single location. The uncertainty represented by the ambiguity of the gradient direction is generally included

in this term. The error caused by incorrect fringe direction estimation is handled as random error.

5. The uncertainty in the absolute values of Ψ. Single interference patterns only contain information regarding $\nabla\Psi$ and not the absolute value of Ψ. Without exact boundary conditions, Ψ cannot be determined in an absolute sense. Experimental evidence for ambient helium permeation is clearly seen in several holographic images - non-zero phase shift appears as low-frequency fringes near the image boundary. As boundary conditions, it is assumed that $\Psi = k$ at the boundaries of the fringe patterns, where k is an uncertain constant, corresponding to the ambient helium concentration around the plume. This process is explained in more detail later on.

Systematic error caused by items 2 and 3 is estimated by manually counting the fringe cycles at certain heights above the helium outlet in a sub-sample (100 frames) of images. This is compared with the number of fringes found by the demodulation algorithm - in other words, the number of 2π discontinuities in a given horizontal phase profile. The difference between the two numbers is averaged over the sub-sample of images and is considered the systematic error at the given height. This bias is removed from the average phase maps and the uncertainty of the bias (the standard deviation of the error) is included as random error. Figure 4 shows the systematic error caused by items 2 and 3, along with the random component as a function of height.

The magnitude of the random error caused by item 4 is estimated based on the time series of Ψ at the sub-sampled grid locations. The unwrapped phase Ψ at a particular location in the plume should exhibit a reasonably smooth, periodic behavior, with the strongest spectral component being the puff frequency. For all cases the time series contains a high-frequency term, with magnitudes usually below 2π. This term was most likely caused by the errors in the direction of $\nabla\psi$. The high-frequency term is separated from the smooth signal by frequency filtering. A low-pass Gaussian kernel is used, with the standard deviation $\sigma = 4f$, where $f = 0.8v_0 Ri^{0.38}/d$, with v_0 being the outlet velocity, Ri is the Richardson

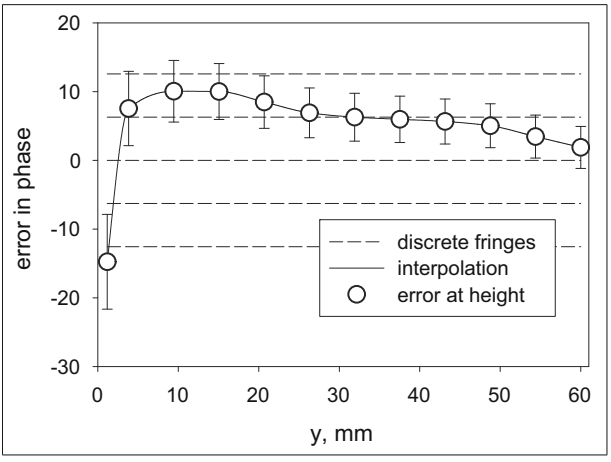

Fig. 4 Systematic error in phase estimation caused by false positive or false negative fringe detection. On average, false negatives dominate close to the outlet, while false positives appear more frequently higher up in the plume. The uncertain systematic error was subtracted from the average phase maps. It is assumed that the systematic error does not depend on the horizontal coordinate

number and d is the outlet diameter [50]. Figure 5 shows the process of estimating the random error caused by the direction ambiguity in ψ.

Different terms in the random error are united by uncertainty propagation. The propagation is performed outside the DC software analysis via Monte-Carlo error propagation. Terms are assumed to be uncorrelated.

2.6 Data consistency

Feeley et al. and Frenklach describe the development of the DC software, and the method is largely developed in the field of combustion kinetics [33, 51], and [52]. DC has potential benefit for the VUQ of all types of mathematical models, but it is applied only sparingly in the field of CFD [53, 54], and [55]. DC requires a thorough consideration of uncertainty from experimental, analytical, and computational data. A lack of information regarding uncertainty can greatly limit what is learned from the DC analysis. For example, if the uncertainty with one or more of the collaborators is too large it is difficult to draw useful conclusions from the data, and while it is easier to demonstrate agreement among data types if the uncertainty is very large, that agreement is less meaningful than if the uncertainties are smaller. Also, as discussed in the simulation section (Section 2.2), it is important to identify the parameters whose uncertainty will likely affect the value of the target quantity the most. Predictions from a CFD model often depend on hundreds of inputs, but the inputs that have the most influence on the target quantity (called the *primary variables*) usually form a

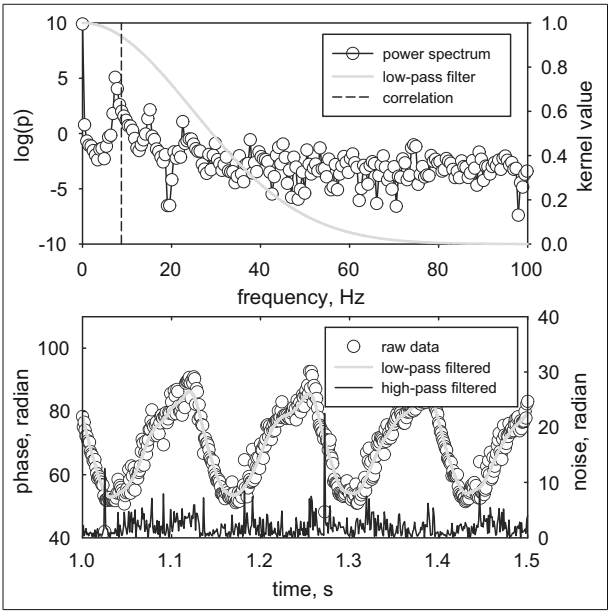

Fig. 5 The estimation of random error caused by the direction ambiguity in ψ. The plots show a single location (center line, 15 mm above outlet) in the plume. Top: power spectrum of time series. The frequency with the highest power is the measured puffing frequency. This experimentally measured frequency is reasonably close to the frequency predicted by empirical correlation (7.3 Hz and 8.7 Hz, respectively) [50]. Bottom: separated smooth and noisy signals. The maximum magnitude of the noisy signal is around 2π radians, which suggests that these noisy observations are indeed caused by direction ambiguity

much smaller subset (two or three variables). In the course of data collaboration, if agreement cannot be shown, a common reason for this is that an important physical phenomenon has not been considered. Often a variable thought to be important initially is subsequently shown through the collaboration process to be of little impact, and such variables must be replaced with more important ones to achieve better agreement between experiment and simulation. To avoid confusion, it is necessary to distinguish between a scenario parameter and a primary variable. The definitions for each of these terms are already given. The parameters listed in Table 1 are all scenario parameters, but they are not all necessarily primary variables. They are variables that the collaborators suspect may be primary variables at the onset of the collaboration. Determination of their status as primary variables occurs as more information presents in the course of the collaboration.

To understand consistency some concepts are necessary. In a collaboration setting the experimentalist attempts to measure the quantity of interest, or the data analyst attempts to extract the quantity of interest from experimental data. The measurement will carry a degree uncertainty defined with an upper and lower bound on the measurement. The computationalist attempts to reproduce the same quantity of interest from simulation. The simulation predictions depend on inputs which also carry uncertainty with upper and lower bounds. The influential model inputs with their uncertainty bounds constitute the model input parameter space. Applying the entire space to the model generates a range of values for the model predictions of the quantity of interest which is comparable to the experimental measurement and uncertainty.

An intuitive definition of consistency is that if there exists a region (no matter how small) in the input parameter space where the model gives predictions that are within the experimental uncertainties for all data points, then the data set is consistent. It is easiest to understand consistency for a data set of only one data point. For such a set if there is overlap between the range of model prediction and the range of experimental uncertainty, then the point is consistent, and if there is no overlap the point is inconsistent. For data sets of multiple points it is more difficult to intuit consistency. It is possible for all data points to show overlap but if the regions of overlap for all the points do not coincide at at least one point in the input parameter space then the whole data set is inconsistent. Details on the DC software can be found at the above cited references (particularly [33].)

Figure 6 summarizes the different aspects of the collaboration process as described thus far.

3 Results from the Collaboration

3.1 Consistency region

The final results of the collaboration are presented first then discussed in detail in later sections. The collaborators find a region of consistency between simulation and experiment. The details of the consistency space are summarized in Fig. 7. The figure shows plot comparisons between prediction and measurement for the first 18 point of the highest level of the plume only (48.99 mm above the inlet.) The comparison is limited to the top level because of the impracticality of presenting all 1296 observed locations and because the data from this level of the plume most clearly present a pattern of discrepancy that is found throughout the upper half of the plume. The other sections of the plume are mostly well-behaved in terms of consistency. Also, only half of the data points (18 out of 36) for the highest level

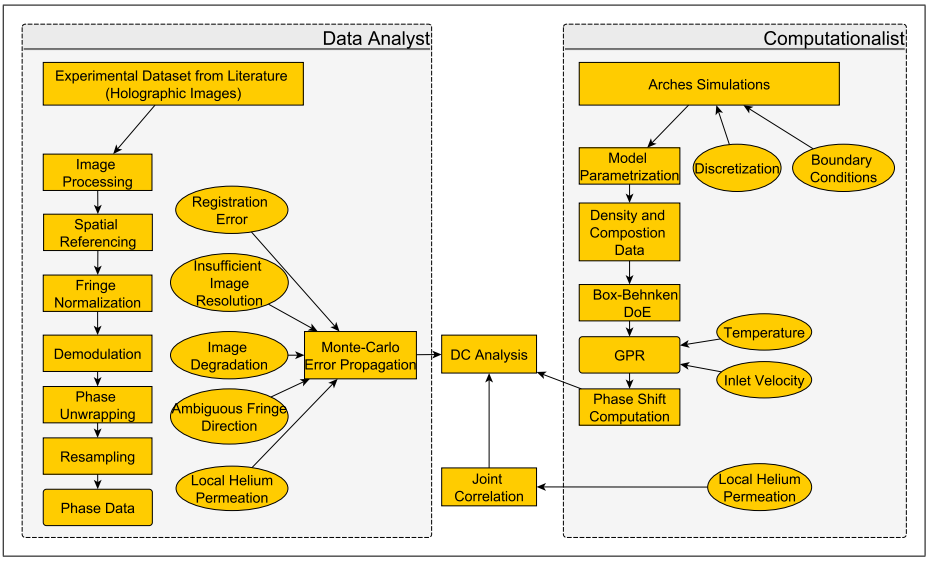

Fig. 6 This diagram illustrates each part of the collaboration process for the laminar helium plume system. The collaboration is divided between the roles of the computatioalist (*on the right*) and the data analyst (*on the left*.) Boxes indicate a step in the processing of the data, and the ovals indicate sources of uncertainty in the analysis

are shown. This is due to an imposed symmetry condition discussed in the next section. Also, corresponding plots of the region of consistency are included with each data comparison. These plots are given at four levels of helium permeation in order to demonstrate how the comparison and consistency change with each level.

In the process of finding this region of consistency, it is found that varying the co-flow velocity has little effect on the agreement between prediction and measurement. All simulations still apply a co-flow boundary, but it is assigned a constant, nominal value and not considered an influential effect on the quantity of interest. A similar conclusion is reached concerning the wavelength of the lab laser. The uncertainty in the wavelength is a reflection of the collaborators ignorance of the laser originally used in the experiments, but the assumed uncertainty in the laser wavelength (reported in Table 1) is too small to have a significant effect on consistency.

In contrast, three of the scenario parameters listed in Table 1 are found to have significant effects on the consistency of the helium data set. These include the system temperature, the helium inlet velocity, and the helium permeation level. The relative importance of each of these input parameters is quantified using the the total effect index as described in [56]. This index accounts for the direct effect of an input on a function as well as any interactions that it has with other inputs (thus the sum of the indices for all the inputs can be larger than one.) In this case the index is computed to measure the effect of each input parameter on the consistency measure (as opposed to the phase shift.) The consistency measure is a concept related to the DC software. It is a quantitative measure of the level of agreement between model predictions and experimental data. The measure carries a value of one, at the highest, for the case of perfect agreement and is negative when the predictions and

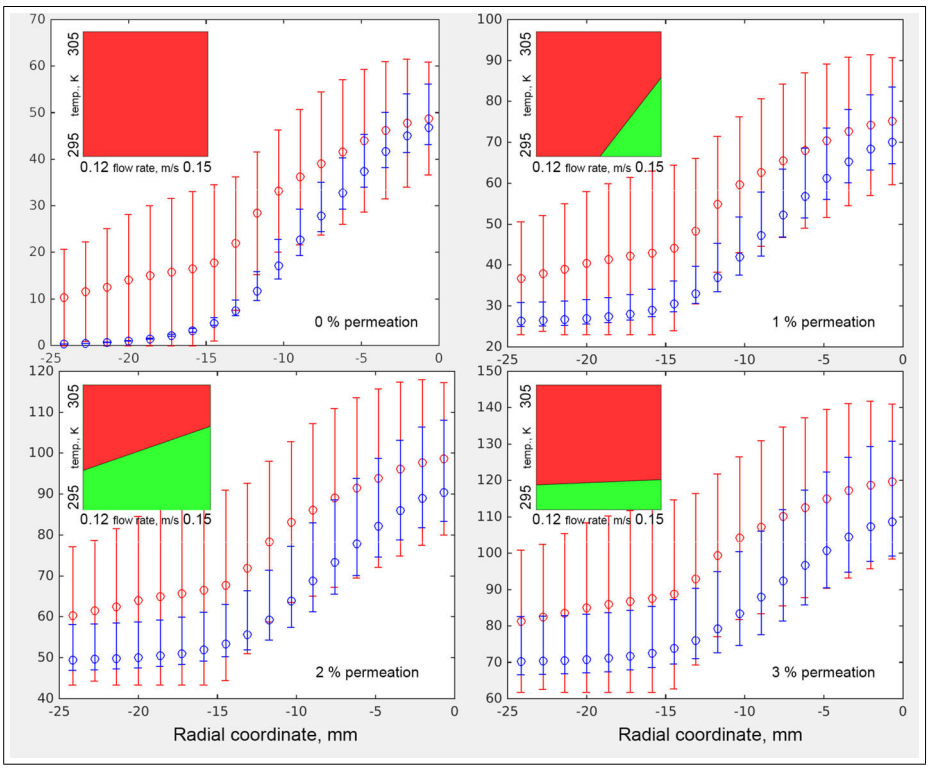

Fig. 7 Comparison plots of phase shift from both simulation (*in blue*) and experiment (*in red*) at different assumed helium permeation levels. The data plotted are from the top observed level of the plume. Only 18 out of 36 points are shown at that level due to imposed symmetry on the data. Each plot also shows a corresponding consistency region (green regions show consistency, red regions show non-consistency)

experimental data are not consistent. By basing the total effect indices on consistency measure, the relative importance of each input parameter to the level of data agreement can be directly estimated. Table 2 reports the total effect indices (as 95 % confidence intervals) for each of the three parameters used in the final analysis of the helium plume. The values indicate that the consistency is most sensitive to system temperature with significant contribution from both helium permeation and inlet velocity.

Table 2 This table summarizes the total effect index for each input parameter used in the final consistency analysis

Parameter	Total effect index (95 % interval)
Temperature	[0.618, 0.630]
Helium inlet velocity	[0.208, 0.212]
Helium permeation	[0.313, 0.321]

The indices are reported as 95 % confidence intervals (based on 50 replicates of each index)

3.2 Plume features examined in the collaboration process

3.2.1 Plume symmetry

In order to achieve the region of consistency shown in Fig. 7, certain conditions and assumptions are made and are described in the following sections. Examination of Fig. 2 shows an important qualitative discrepancy between the observed plume and the computational plume. The holographic image shows a plume with fringe lines that extend further to the left that they do to the right. Also, at the bottom of the plume, near the inlet, there is a "dome" of fringe lines that tend to lean to the left. In contrast to the asymmetric character of the plume observed in the hologram, the fringe line patterns of the computationally generated plume show virtually perfect symmetry. This qualitative difference between the two plumes makes it impossible to do meaningful comparison between the data types or to find a region of consistency.

Figure 8 illustrates another important clue in the behavior of the plume. This figure shows a series of holographic interferograms in sequence confined to the time frame of one puff of the plume. In this series of images a "bubble" forms at the base of the plume on the left side and travels upward. When the bubble reaches the upper-left section of the plume it "pushes" the helium out to greater radial distances, and it pushes the center of the plume slightly to the right of the center line. The formation of this bubble correlates with much of the asymmetric character of the observed plume. The fringes surrounding this bubble show more separation among themselves than the fringes on the right side of the plume. In fact, an unusual separation of fringe lines is what defines the bubble. The separation of fringe lines as well as the presence of thicker fringes indicate that the concentration gradient of

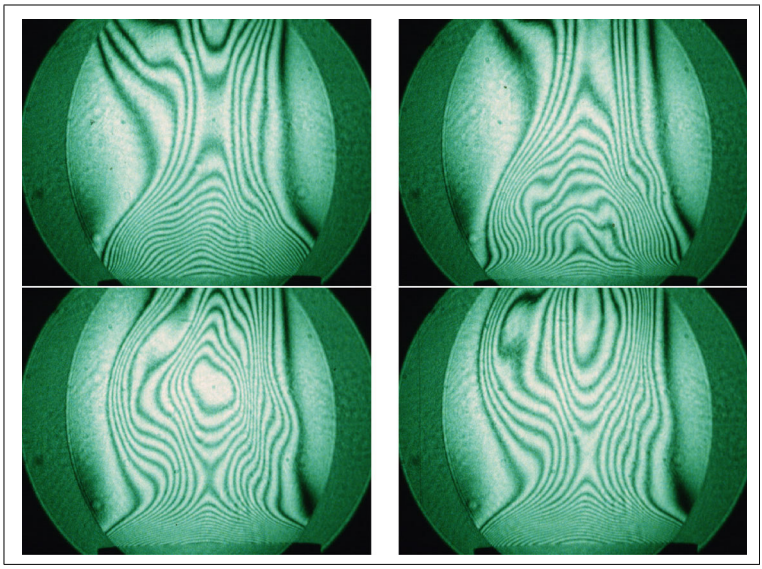

Fig. 8 Four examples of the holographic interferograms of the helium plume showing the asymmetric character of the plume as it progresses

helium in this section of the plume is much lower than that on the right side. Entrainment of air from the surroundings, some kind of baffling obstruction in the inlet port, or an air leak in the port are all possible explanations for the formation of this bubble. The bubble formation and propagation shown in Fig. 8 repeats in other images from the experiment.

A number of other likely causes for the asymmetric character of the experimentally observed plume include: asymmetry in the helium inlet velocity profile and asymmetric air currents and pressures in the surrounding environment. Regardless of the cause of the asymmetry, it is important to note that it is the computational plume that is unusual. The asymmetries in the observed plume are common among buoyant plumes observed in experimental conditions [28] and [39]. Therefore, the source of the discrepancy between experiment and simulation is likely an inadequate accounting for the open system conditions from the experiment in the helium simulations.

The co-flow and pressure boundary conditions are applied to capture the effects of an open system for the simulated plume, but the results suggest that these measures are insufficient. A large number of simulations are run to attempt to capture the asymmetry of the plume. These include imposing an asymmetric helium inlet that favors the left side to varying degrees, imposing crosswind conditions, inserting a baffle at the entrance of the inlet, setting different co-flow velocities on the left and right sides of the plume, etc. All of these computational experiments produce results that fail to produce consistency in the data set or to capture the observed phenomena in the plume. It is thought that the only way to properly capture the asymmetric qualities in the plume is to include more of the surrounding domain in the simulations. Perhaps it is necessary to include the entire room where the experiments occur. It is difficult to tell what conditions in the room could impact the flow behavior of the plume: an air or intake vent, sunlight or other heat source, an opening or closing door, or a person pacing around the room. Any disturbance could induce small currents and pressure changes in the room which all could affect the plume. There are at least two problems with including this type of domain in the simulation: (1) the exact layout of the room and detailed information on what happens during the experiment are not known, and (2) even if they were known, there is insufficient computational resource to simulate such a large, complex domain with sufficient resolution.

Instead of including the larger system in the simulations it is easier to treat the surrounding flow patterns and the circumstances of the experiments as unknown conditions with an effect on the uncertainty of the experimental data. This is done by imposing a symmetry condition on the unwrapped phase shift data from the holographic interferograms. Symmetry is imposed by examining each data point and the point opposite on the other side of the center and unifying the two points by determining the maximum and minimum values allowed in the uncertainty ranges of both points. The maximum and minimum uncertainties are then applied to both points, and the center of the new range becomes the nominal value. This way both data points of equal distance from the center are exactly the same, with the same measurement and the same expanded uncertainty range. Since the data from both simulation and experiment are now made symmetric it is only necessarily to look at one side of the plume for consistency analysis as reflected in the data comparisons in Fig. 7. This procedure is applied to all 1296 data points in the data set. At this point both the computational and experimental data are now symmetric and can be more easily compared for consistency analysis. This is done at the expense of enhancing the error associated with the experimental data, which potentially limits the ability of the collaborators to find meaningful agreement in the data.

3.2.2 *Local helium permeation*

In addition to the assumption of plume symmetry, it also necessary to consider that helium permeates the region just beyond the column of the plume in order to achieve the consistency region shown in Fig. 7. The data comparison for 0 % helium permeation (top-left section of Fig. 7) shows weak agreement between prediction and measurement at the data points about half-way between the center of the plume and the edge. Also, the corresponding consistency map shows no region of consistency possible when there is zero helium in the immediate region around the plume.

The presence of helium in the air surrounding the plume would cause a drop in density for that region. This lower density means that the density difference between the plume and the surrounding fluid is also smaller, leading to diminished plume buoyancy. For a scenario where helium permeates the immediate surroundings, the same inlet inlet flow rate with decreased buoyancy would result in the helium pushing radially outward, thus producing a wider plume. This is consistent with the observations from the holographic interferograms showing a wider plume than that predicted from simulation where the surrounding fluid is modeled as pure air. Also, there is evidence in the holographic images of helium outside the main column of the plume. Examination of the holographic images in Figs. 2 and 8 shows a large, diffuse fringe on the left edge of the images. The appearance of such a fringe occurs only if additional phase shift occurs outside the column of the plume, and the presence of helium at that location is the most likely reason.

To investigate the effect of local helium permeation another simulation is performed that includes helium in the immediate surroundings. To include this phenomenon, the simulation assigns an initial concentration of 0.3 % helium (by mass) to the entire domain, and the co-flow inlet contributes the same concentration to the mass it injects into the domain. Figure 9 shows the difference in the phase shifts for the 0.3 % permeation case and a similar simulation with pure air. It shows that helium permeation increases the phase shift everywhere. This is expected as the object beam from the experiment would encounter not only helium in the plume but also in the area surrounding the plume as well, thus creating a larger phase shift. This also assumes that the air inside the reference beam tube is pure, which is likely because the reference beam is separated from the plume. It is important to emphasize that for helium permeation to affect the phase shift results it need not fill the whole room. Helium permeation adjacent to the plume column is all that is required. Figure 9 also indicates that the change in phase shift is not uniform over the whole plume. The regions where helium is already abundant before the inclusion of local permeation (i.e. the center and base of the plume) show a smaller increase in phase shift than the regions that previously contain pure air. This means the the inclusion of helium permeation produces at least two effects on the simulated data: (1) The values of the phase shift will increase with increasing helium concentration levels (i.e. the phase shift data will translate upwards), and (2) the increase in phase shift varies over the area of the plume. Since the phase shift increase is smaller at the center of the plume than at the edges of the plume, this results in a phase shift profile that is broader than initially predicted in simulation with no helium permeation. The computational plume then appears more like the observed plume in the holographic images.

Local helium permeation also affects the experimentally determined phase shift values. As discussed in Section 2.5, in order to generate meaningful phase data from the holographic interferograms that are comparable with the simulation data, a simple instrument model processes the raw phase data by locating the minimum value of phase and assuming that this

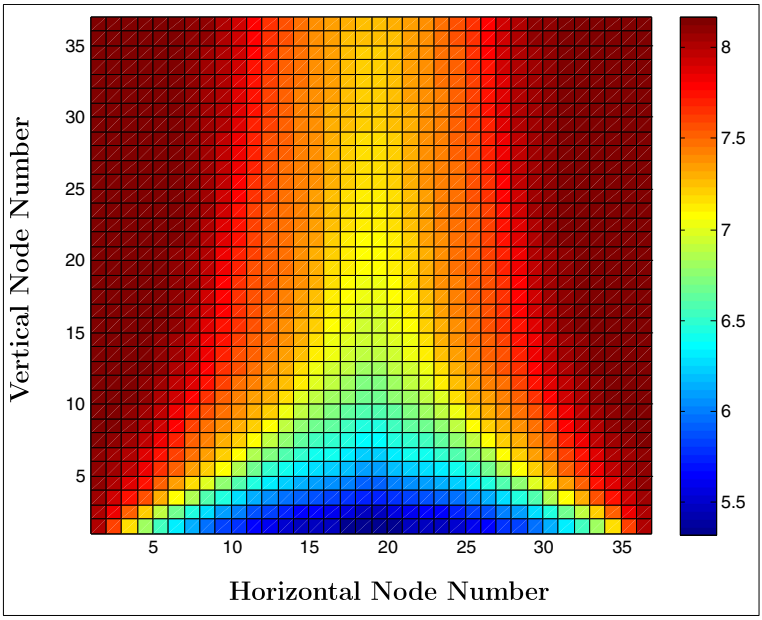

Fig. 9 This color plot shows the difference in time-averaged phase shifts predicted between two simulations. The simulations are the same except one assumes the region near the plume is pure air, and the other assumes that the same region has a base helium concentration of 0.3 % by mass. Each square in the plot represents a computational node in the simulation domain. The image is centered with the plume. Each node has dimensions of 0.138 by 0.138 centimeters. Thus the image covers 4.968 by 4.986 centimeters about the plume

value corresponds to a region of pure air. The instrument model adjusts the minimum phase shift to a value of zero and adjusts all other phase values accordingly. With the possibility of helium permeation, the assumption of pure air at the location of minimal phase shift is no longer certain. The instrument model must now allow for the possibility of the minimum phase value corresponding to some value other than zero. Because the relative values of the experimentally determined phase shifts are fixed, the effect of helium permeation on the experimental data is a pure translation. Higher assumed values in the surrounding helium concentration level produce higher the values in phase shift from the image processing.

One approach to handling helium permeation is to include it in the simulations using values ranging from 0% to 0.3% (helium by mass.) Also, the data analyst must also treat helium permeation as a source of uncertainty, using the same range of values for permeation as in the simulations. With helium permeation considered in this manner the uncertainty ranges for both data types increase significantly producing a strong consistency region.

However, it is thought that there are problems in applying local helium permeation in this manner. Permeation affects the analysis in a way that no other previously considered scenario parameter does. Local helium permeation could be called a *shared variable*. Such a variable impacts uncertainty in the experimental data (in this case through the instrument model), and it impacts the uncertainty in the computational data as well. However, to simply allow this parameter to inflate both uncertainty ranges may produce a false indication of consistency. For example, it is possible to form a point of consistency where the value

of phase shift from the simulation may arise from one value of helium permeation (say 0.15 %), and the experimental uncertainty may arise from the possibility that the permeation is a completely different value (say 0.25 %). Treating the uncertainty from a shared variable in this manner would produce the appearance of consistency where none exists. Therefore in dealing with a shared variable it is important to ensure that its value correlates between the simulation and the instrument model. If an alleged region of consistency is to be considered valid the shared variable must have the same value for both the CFD model and the instrument model.

3.2.3 Correlating helium permeation

A second approach to the consistency analysis requires correlation of the helium permeation between the data analyst's output and simulation prediction in all comparisons. To do this it is necessary to upgrade the instrument model to process the unwrapped phase shift data and adjust it based on a given level of permeation. The model simply translates the phase shift values depending on the degree of assumed permeation, but determining to what degree the data should translate depends on a conceptual model of the permeation zone near the plume. The conceptual model copies the approach in the simulations. It calculates the phase shift for a portion of the laser beam that does not pass through the helium plume. The beam follows a path through the permeation zone that is 13.8 centimeters (the same dimension used in the simulation domain.) The instrument model assumes that all helium that the object beam encounters from its inception to the point of combination with the reference beam is contained in this region. The helium concentration is assumed constant along this path. With the application of these assumptions a phase shift is computed using Eqs. 1 and 5. The resulting value is the minimum phase shift, and it is used to translate the processed experimental phase data set. The model assumes an unlikely distribution (a uniform distribution) of helium in the permeation zone. There is no way for the collaborators to know the exact size and concentration distribution of the actual permeation zone. The approach uses a simple, uniform model of the permeation zone to generate an equivalent phase shift to that occurring in the actual plume. The assumed helium concentration correlates to the path-averaged concentration in the actual permeation zone in the experiment.

In this approach to applying the local helium permeation to the consistency analysis a value for the helium level is chosen. The instrument model adjusts the processed experimental data according to the chosen permeation level, and simulation data allow variation in helium inlet velocity, and the system temperature, but the helium level remains fixed at the chosen value. This way the comparison keeps the local permeation level congruent for both data types, and this avoids the possibility of false consistency results. The collaborators use a helium range from 0 % to 3 %. This upper limit is an arbitrary value based on what the collaborators consider to be the likely local permeation levels reached in this scenario.

The approach of doing separate consistency analyses for each level of helium permeation is reflected in the organization of the results shown in Fig. 7. At each investigated level of helium permeation both the experimental and computational data change, and the degree of agreement between the two also change. Without helium permeation, there is no combination of system temperature and inlet velocity that gives consistency with the experimental data. A region of consistency in the input parameter space forms near 1 % permeation. That region gets larger near 2 % before shrinking as helium permeation approaches 3 %. The first method of applying the effect of permeation to the error of both data types indicates consistency at permeation levels well under 1 %. By enforcing the same helium permeation level in both data types, the region of consistency occurs at a higher permeation level. This

supports the idea that false consistency can occur with the first method, and it suggests preference for the correlated method.

4 Conclusions and Future Work

The important goal for model VUQ is not to claim a validated model. What is important is what is learned about the code, the experiment, the data processing, and the physical system in the model VUQ process. The collaboration provides information on the limitations of the code as used in the study. The limitations relate to the boundary conditions applied in the simulations to produce the effects of an open room environment. The collaboration process reveals that these boundary conditions are insufficient to reproduce the effects of the open room on the plume. This process also sheds light on how much progress there remains to be done in achieving thorough quantitative model VUQ. Despite the absence of error-prone models (turbulence, reaction kinetics for example), the experimental conditions (i.e. natural air currents in a common lab) create enough difficulty in matching the predictions with experiment. The open system condition becomes more pronounced in fluid systems in outdoor environments. The only ways to treat this phenomenon more rigorously are to either simulate the entire room (or enough of the room) or place more control on the experimental conditions to make the plume easier to simulate.

The results from the collaboration show that once uncertainty is properly accounted in the experimental data and important physical phenomena are included in the simulations, Arches produces results that meet consistency criteria for the laminar helium plume case, and this constitutes a measure of quantitative agreement between the data types. However given the amount of uncertainty added to the experimental data due to the asymmetric conditions that the model could not capture and also due to a lesser degree from the possibility of local helium permeation, there is a question of how meaningful this agreement is. Without capturing the full asymmetry of the plume it would be premature to claim that the code is validated for the laminar helium system presented here.

The collaboration process also demonstrates the need for collaborators to recognize the parameters that have the most influence on the system and the quantities of interest. This is perhaps the greater contribution of this study for buoyant plume systems: the identification of the primary variables and the determination of their relative importance as summarized in Table 2.

The collaboration also reveals that certain phenomena like local helium permeation can affect both computational and experimental methods, and that the uncertainty associated with such phenomena must be handled carefully so that a false indication of data agreement does not influence the results.

Even without the use of large collections of data on the system of interest or the comparison of numerous CFD codes trying to simulate the same system, this smaller-scale collaboration with a simple system demonstrates a powerful means of gleaning a better understanding of the physics of that system and also a better understanding regarding the strengths and limitations of the tools the collaborators employ. This also helps improve understanding of more complex systems like turbulent pool fires, industrial flares, drag on an aircraft or road vehicle, vortex formation with air craft, etc.

Finally, the scope of the collaboration demonstrated in this study is limited in terms of the role of the experimental team. Full participation of an experimental team would allow the collaborative effort more tools in dealing with the problems of plume asymmetry and

helium permeation. For example changes to the experimental setup could produce symmetric data that are more suitable for comparison with computational predictions. Similarly, changes to the experimental design could ensure that unintended helium permeation is minimized. Also, efforts at additional measurement could provide the simulation team with better boundary conditions that would improve predictions. Despite the limitations of the collaboration shown in this study, it does have advantages over the more experimental-involved model of collaboration. Having a full experimental team on hand that can return to the lab and take additional measurements according to the needs of the collaboration is much more costly and labor intensive. In many cases this capability is not practical or even possible. Such cases where good literature data is available but a flexible experimental team is not available, the present collaborative model shows a valid approach to gleaning additional, valuable information from the data that would not be possible if each party worked alone.

Acknowledgments This material is based upon work supported by the Department of Energy under Award Numbers DE-NT0005015, DE-NA0000740, and CSAFE (contract No. LL B341493.) The views and opinions of authors expressed herein do not necessarily state or reflect those of the United States Government or any agency thereof.

Compliance with Ethical Standards This study has been conducted according to SCOPE guidelines. To the author's knowledge there are no conflicts of interest (financial or otherwise, direct or indirect), and no human or animal experimentation is involved.

References

1. East, E.W., Kirby, J.G., Liu, L.Y.: Verification and validation of a project collaboration tool. Autom. Constr. **17**, 201–214 (2008)
2. Hills, R.G., Leslie, I.H.: Statistical validation of engineering and scientific models: Validation experiments to application. Tech. Rep. SAND2003-0706 Sandia National Laboratories (2003)
3. Oberkampf, W., Trucano, T.: Verification and validation in computational fluid dynamics. Prog. Aerosp. Sci. **38**, 209–272 (2002)
4. Oberkampf, W.L., Barone, M.F.: Measures of agreement between computation and experiment: Validation metrics. J. Comput. Phys. **217**, 5–36 (2006)
5. Rebba, R., Mahadevan, S.: Computational methods for model reliability assessment. Reliab. Eng. Syst. Saf. **93**, 1197–1207 (2008)
6. Roache, P.J.: Quantification of uncertainty in computational fluid dynamics. Annu. Rev. Fluid Mech. **29**, 123–160 (1997)
7. Roache, P.J.: Verification and Validation in Computational Science and Engineering Hermosa Publishers (1998)
8. Choi, S., Garcia, M.H.: κ-ϵ turbulence modeling of density currents developing two dimensionally on a slope. J. Hydraul. Eng. **128**, 55–63 (2002)
9. DesJardin, P.E., O'Hern, T.J., Tieszen, S.R.: Large eddy simulation and experimental measurements of the near-field of a large turbulent helium plume. Phys. Fluids **16**, 1866–1883 (2004)
10. Gandhir, A., Hassan, Y.: RANS modeling for flow in nuclear fuel bundle in pressurized water reactors (PWR). Nucl. Eng. Des. **241**, 4404–4408 (2011)
11. Hsaio, S., Lin, T.: Tsunami-like solitary waves impinging and overtopping an impermeable seawall: Experiment and RANS modeling. Coast. Eng. **57**, 1–18 (2010)
12. Hu, L.Y., Zhou, L.X., Zhang, J.: Large-eddy simulation of a swirling diffusion flame using a SOM SGS combustion model. Numer. Heat Transfer, Part B **50**, 41–58 (2006)
13. Jiang, Y., Chen, Q.: Effect of fluctuating wind direction on cross natural ventilation in buidlings from large eddy simulation. Build. Environ. **37**, 379–386 (2002)

14. Kartushinsky, A., Michaelides, E.E., Rudi, Y., Nathan, G.: RANS modeling of a particulate turbulent round jet. Chem. Eng. Sci. **65**, 3384–3393 (2010)
15. Ma, J., Oberai, A.A., Drew, D.A., Lahey, R.T., Hyman, M.C.: A comprehensive sub-grid air entrainment model for RANS modeling of free-surface bubbly flows. Journal of Computational Multiphase Flows **3**, 41–56 (2011)
16. Paik, J., Eghbalzadeh, A., Sotiropoulos, F.: Three-dimensional unsteady RANS modeling of discontinuous gravity currents in rectangular domains. J. Hydraul. Eng. **135**, 505–521 (2009)
17. Tominaga, Y., Stathopoulos, T.: CFD simulation of pollution dispersion in a street canyon: comparison between LES and RANS. J. Wind Eng. Ind. Aerodyn. **99**, 340–348 (2011)
18. Abecassis-Empis, C., Reszka, P., Steinhaus, T., Cowlard, A., Biteau, H., Welch, S., Rein, G., Torero, J.L.: Characterization of Dalmarnock fire test one. Exp. Thermal Fluid Sci. **32**, 1334–1343 (2008)
19. Barley, C.D., Gawlik, K.: Buoyancy-driven ventilation of hydrogen from buildings: Laboratory test and model validation. Int. J. Hydrogen Energy **34**, 5592–5603 (2009)
20. Blanchat, T.K., Nicolette, V.F., Sundberg, W.D., Figueroa, V.G.: Well-characterized open pool experiment data and analysis for model validation and development. Tech. Rep. SAND2006-7508, Sandia National Laboratories (2006)
21. Coustols, E., Jacquin, L., Schrauf, G.: Status of wake vortex alleviation in the framework of european collaboration: Validation attempts using tests and CFD results. In: European Conference on Computational Fluid Dynamics (2006)
22. Frenklach, M.: Transforming data into knowledge – process informatics for combustion chemistry. Proc. Combust. Inst. **31**, 125–140 (2007)
23. O'Hern, T.J., Weckman, E.J., Gerhart, A.L., Tieszen, S.R., Schefer, R.W.: Experimental study of a turbulent buoyant helium plume. J. Fluid Mech. **544**, 143–171 (2005)
24. Welch, S., Jowsey, A., Deeny, S., Morgan, R., Torero, J.L.: BRE large compartment fire tests – characterising post-flashover fires for model validation. Fire Saf. J. **42**, 548–567 (2007)
25. Ahn, J.W., ho Kim, J., Kim, C., hyun Cho, J., Hur, C., Kim, Y., hyun Kang, S., Kim, B., Moon, J.B., Cho, K.W.: Future application and middleware technology on e-science, chap. Web-based integrated research environment for aerodynamic analyses and design, pp. 1–10. Springer (2010)
26. Crowther, W.J., Lunnon, I., Wood, N.J., Davies, A.G., Hurst, D., Coulton, D.G.: A grid enabled wind tunnel test system (GEWiTTS): Toward real time integration of CFD and experiment. In: Proceeding of the 2nd Integrating CFD and Experiment in Aerodynamics international symposium (2005)
27. Vassberg, J.C., Tinoco, E.N., Mani, M., Levy, D., Zickuhr, T., Mavriplis, D.J., Wahls, R.A., Morrison, J.H., Brodersen, O.P., Eisfeld, B., Murayama, M.: Comparison of NTF experimental data with CFD predictions from the Third AIAA CFD Drag Prediction Workshop. In: Summary of the Third AIAA CFD Drag Prediction Workshop (2008)
28. Kaufmann, M.: Dimensionslose kennzahlen und grenzschicht-schwingungen bei auftriebsbehafteten diffusionsflammen und nicht-reagierenden strmungen. [dimensionless characteristic numbers and oscillations of thermal boundary layers in buoyant pool flames and in non-reacting flows(helium plumes.)]. Ph.D. thesis University of Stuttgart (1990)
29. Burton, G.C.: Large-eddy simulation of a turbulent helium-air plume using the nLES method. Tech. rep., Center for Turbulence Research Stanford University and NASA-Ames Research Center (2009)
30. Chung, W., Devaud, C.B.: Buoyancy-corrected k-e models and large eddy simulation applied to a large axisymmetric helium plume. Int. J. Numer. Methods Fluids **58**, 57–89 (2008)
31. Maragkos, G., Rauwoens, P., Wang, Y., Merci, B.: Large eddy simulations of the flow in the near-field region of a turbulent buoyant helium plume. Flow Turbul. Combust. **90**, 511–543 (2013)
32. Spinti, J., Thornock, J., Eddings, E., Smith, P., Sarofim, A.: Transport phenomena in fires, chap. Heat transfer to objects in pool fires, pp. 69–136. WITpress, Boston (2006)
33. Feeley, R., Seiler, P., Packard, A., Frenklach, M.: Consistency of a reaction dataset. J. Phys. Chem. **108**, 9573–9583 (2004)
34. Schönbucher, A., Arnold, B., Banhardt, V., Bieller, V., Kasper, H., Kaufmann, M., Lucas, R., Schiess, N.: Simultaneous observation of organized density structures and the visible field in pool fires. In: Twenty-First Symposium (International) on Combustion/ The Combustion Institute, pp. 83–92 (1986)
35. Wolfram—Alpha knowledgebase,.: July 10, 1984 stuttgart, germany. Online (2010). http://www.wolframalpha.com/input/?i=july+10,+1984+stuttgart+Germany
36. Wilke, C.R., Lee, C.Y.: Estimation of diffusion coefficients for gases and vapors. Ind. Eng. Chem. **47**, 1253–1257 (1955)
37. Box, G.E., Behnken, D.W.: Some new three level designs for the study of quantitative variables. Technometrics **2**, 455–475 (1960)
38. Rasmussen, C.E., Williams, C.K.I.: Gaussian processes for machine learning the MIT Press (2006)

39. Gawlowski, M., Kelly, K.E., Marcotte, L.A., Schönbucher, A.: Determining the effect of species composition on temperature fields of tank flames using real-time holographic interfereometry. Appl. Opt. **48**, 4625–4636 (2009)
40. Jiang, Z.: Reliable validation based on optical flow visualization for CFD simulations. Acta Mech. Sinica **19**, 193–203 (2003)
41. Lucas, R.: Holografische synchroninterferometrie zur untersuchung von tankflammenfeldern und ihren kohrenten strukturen [holographic real-time interferometry for the investigation of tank flames including coherent fluid dynamic structures.]. Ph.D. thesis University of Stuttgart (1981)
42. Lucas, R., Broetz, W., Schönbucher, A.: Interferometrische synchronfotografien zur untersuchung turbulenter vorgnge in tankflammen.[hologaphic interference patterns for investigation of turbulent phenomena in tank flames.] Berichte der Bunsengesellschaft fr physikalische Chemie **82**, 189–192 (1978)
43. Schönbucher, A.: Waerme-,stoff-und impulstransportvorgaenge unter beruecksichtigung kohaerenter strukturen in tankflammen organischer fluessigkeiten.[heat-,mass-and momentum transfer processes including coherent fluid dynamic structures in tank flames.]. Fortschritt-Berichte VDI-Z 6(83) (1981)
44. Servin, M., Quiroga, J.A., Marroquin, J.J.: General n-dimensional quadrature transform and its application to interferogram demodulation. J. Opt. Soc. Am. A **20**, 925–934 (2003)
45. Larkin, K.G., Bone, D.J., Oldfield, M.A.: Natural demodulation of two-dimensional fringe patterns. i. general background of the spiral phase quadrature transform. J. Opt. Soc. Am. A **18**, 1862–1870 (2001)
46. Villa, J., la Rosa, I.D., Miramontes, G., Quiroga, J.A.: Phase recovery from a single fringe pattern using an orientational vector-field-regularized estimator. J. Opt. Soc. Am. A **22**, 2766–2773 (2005)
47. Guerrero, J.A., Marroquin, J.L., Rivera, M., Quiroga, J.A.: Adaptive monogenic filtering and norMalization of ESPI fringe patterns. Opt. Lett. **30**, 3018–3020 (2005)
48. Pritt, M.D.: Phase unwrapping by means of multigrid techniques for interferometric SAR. IEEE Trans. Geosci. Remote Sens. **34**, 728–738 (1996)
49. XtremeFringe: Fringe pattern processing library Online (2011). http://www.iot.es/ingles/xtreme.html
50. Cetegen, B.M., Kasper, K.D.: Experiments on the oscillatory behavior of buoyant pumes of helium and helium-air mixtures. Phys. Fluids **8**, 2974–2984 (1996)
51. Feeley, R., Frenklach, M., Onsum, M., Russi, T., Arkin, A., Packard, A.: Model discrimination using data collaboration. J. Phys. Chem. **110**, 6803–6813 (2006)
52. Frenklach, M., Packard, A., Seiler, P., Feeley, R.: Collaborative data processing in developing predictive models of complex reaction systems. Int. J. Chem. Kinet. **36**, 57–66 (2003)
53. Eldredge, W.M., Thornock, J.N., Smith, P.J.: Develpment, verification, and validation of the responsive boundary model for pool fire simulations. In: 20th AIAA Computational Fluid Dynamics Conference (2011)
54. Sheen, D.A., Wang, H.: The method of uncertainty quantification and minimization using polynomial chaos expansions. Combust. Flame **158**, 2358–2374 (2011)
55. Pedel, J., Thornock, J.N., Smith, P.J.: Ignition of co-axial turbulent diffusion oxy-coal jet flames: Experiments and simulations collaboration. Combust. Flame **160**, 1112–1128 (2013)
56. Saltelli, A., Annoni, P., Azzini, I., Campolongo, F., Ratto, M., Tarantola, S.: Variane based sensitivity analysis of model output. design and estimator for the total sensitivity index. Comput. Phys. Commun. **181**, 259–270 (2010)